INSTITUTE OF PHYSICS PUBLISHING JOURNAL OF MICROMECHANICS AND MICROENGINEERING
J. Micromech. Microeng. **12** (2002) 862–869 PII: S0960-1317(02)37632-0

PIV measurements in a microfluidic 3D-sheathing structure with three-dimensional flow behaviour

H Klank[1], G Goranović[1], J P Kutter[1], H Gjelstrup[2], J Michelsen[2] and C H Westergaard[3]

[1] MIC-Mikroelektronik Centret, μTAS Project, Technical University of Denmark, 2800 Lyngby, Denmark
[2] Department of Mechanical Engineering, Fluid Mechanics Section, Technical University of Denmark, 2800 Lyngby, Denmark
[3] Dantec Dynamics A/S, Tonsbakken 16-18, 2740 Skovlunde, Denmark

E-mail: hk@mic.dtu.dk and carsten.westergaard@dantecdynamics.com

Received 31 May 2002, in final form 2 September 2002
Published 3 October 2002
Online at stacks.iop.org/JMM/12/862

Abstract
The design and production time for complex microfluidic systems is considerable, often up to several months. It is therefore important to be able to understand and predict the flow phenomena prior to design and fabrication of the microdevice in order to save costly fabrication resources. The structures are often of complex geometry and include strongly three-dimensional flow behaviour, which poses a challenge for the micro particle image velocimetry (micro-PIV) technique. The flow in a microfluidic 3D-sheathing structure has been measured throughout the volume using micro-PIV. In addition, a stereoscopic principle was applied to obtain all three velocity components, showing the feasibility of obtaining full volume mapping (x, y, z, U, V, W) from micro-PIV measurements. The results are compared with computational fluid dynamics (CFD) simulations.

(Some figures in this article are in colour only in the electronic version)

1. Introduction

Along with the requirements for more advanced liquid handling capabilities, the layout of microstructures becomes more and more complex. Computer modelling can accelerate and help in the labour intensive and time consuming process of intuitive design, fabrication and testing. However, in order to use simulations reliably as a design tool, the software used for modelling must initially be validated experimentally, e.g. with particle image velocimetry (PIV).

A microstructure that allows coaxial sheathing of a sample stream with a buffer stream was chosen as a demonstrator and is shown in figures 1 and 2. This so-called chimney structure is a crucial part of a micro cell sorter (Wolff *et al* 2000). The purpose of the cell sorter is to select cells according to specific biochemical and physical properties, e.g. whether they are leukaemia cells, or according to their size. For the cells to be recognized and selected, they have to be marked with fluorescent labels before they can be detected by the system. The detection system is typically organized like an epi-fluorescent microscope.

In a conventional cell sorter the sample fluid containing the labelled cells enters the sorter centrally in such a way that a buffer stream surrounds the sample. This sheathing of the sample ensures that cells are only travelling within the very narrow field of view of the detection system. Sheathing can only work under laminar flow conditions, which prevents the premature mixing of buffer and sample.

The type of sample sheathing as described above is difficult to achieve within micro cell sorters due to the two-dimensional, planar character of the fabricated devices. First-generation micro cell sorters therefore reverted to using two-dimensional sample sheathing. Such sample sheathing, however, has the disadvantage of signal and speed variations. Since the sample is neither sheathed on top nor sheathed on the bottom, cells can travel at any height within the fluidic

 © 2002 IOP Publishing Ltd Printed in the UK

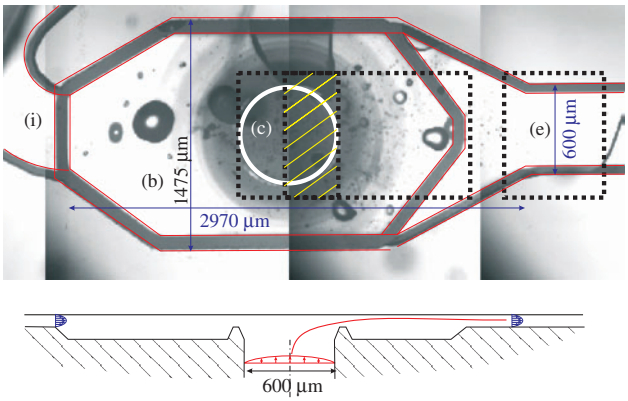

Figure 1. Overview of the chimney structure. The laminating buffer flow is entering the basin (b) from the left through the inlet (i), while the sample flow is entering the basin through the centre of the chimney (c). The total flow is leaving the basin over a step into the exit channel (e), where the lamination of the samples is completed. PIV measurements were performed in the outlined dashed areas. Stereoscopic PIV recombination was performed in an overlapping area from two camera positions over the chimney entrance, as indicated by shading.

channel of the micro cell sorter. Cells travelling outside the focal plane of the detection system will generate a lower signal than those travelling within the focal plane. Cells will also travel at different speeds due to the parabolic flow profile that develops in the channel. These speed differences diminish the accuracy of the cell sorter. To overcome these two disadvantages, second-generation micro cell sorters were developed that were able to sheath the sample three dimensionally, for example by Larsen (2000) and Tashiro *et al* (2000). The chimney structure, which has been developed at MIC (Larsen 2000) and is discussed in this paper, used only one input for the buffer to achieve coaxial sheathing of the sample. The chimney structure was described in more detail by Goranović *et al* (2001). It should be noted that the flow within a microfluidic system is always laminar under all practical conditions due to the extraordinary low Reynolds numbers. The above mentioned condition for a cell sorter that the sheathing flow should always be laminar is therefore fulfilled in all microfluidic cell sorters.

As shown in figures 1 and 2, the chimney structure consists of an inlet channel, the chimney itself, a basin and an exit channel. The sheathing buffer flow enters the basin through the inlet channel, where it merges with the sample flow entering through the chimney. The sheathing of the sample is gradually completed as the fluids exit through the outlet channel. The chimney basin was designed to take care of the laminating part of the buffer stream underneath the sample stream. At the end of the basin, the reduction in cross sectional area leads to an increase in flow velocity, which is especially high just at the basin corner. This layer of high-velocity buffer stream ensures sheathing at the bottom of the sample stream. Sheathing at the top of the sample stream is ensured as long as the buffer stream is fast enough to avoid being pushed backwards by the incoming sample stream.

Particle image velocimetry (PIV) has been applied in a number of microscopic devices with nozzle- or channel-like shapes, for instance by Meinhart *et al* (1999). In micro-PIV, where microscopes are used for imaging, all three important variables, spatial resolution, the equivalent of the light sheet thickness and field of view, are intertwined. The micro-PIV technique therefore has to balance these variables. Especially, the chimney structure provides additional challenges, since the structure is characterized by a complex geometry with a strongly three-dimensional flow.

The flow is visualized in figure 2 by introducing a tracer into the sample flow. The strongest out-of-plane movement is found near the outlet of the chimney and at the exit of the basin.

2. Experimental set-up

The chimney structure was fabricated in silicon by reactive ion etching. The top of the structure was closed with a glass cover, which was bonded directly to the silicon. The thickness of the cover glass was 0.75 mm. The fluid was purified water, which for the purpose of the PIV measurement was seeded with 1.0 μm 'orange fluorescent' polystyrene particles (Fluospheres, Molecular Probes). The excitation maximum of these particles was at around 540 nm, while the emission maximum was at around 560 nm. Sample and buffer were infused with one syringe pump (Pump 22, Harvard Apparatus) each. The flow rate for the sample flow through the chimney was kept constant at 0.02 ml min^{-1}, while the flow rate of the laminating flow was varied. Three flow cases were investigated giving a volume flow ratio of $R = 0.5$, 5 and 25, where R is the ratio of the laminating flow over the sample flow, also shown in table 1. The coordinates were placed with their origin in the centre of the chimney and the z-axis pointing out of the structure. The y-axis was positive in the main flow direction.

A Dantec HiSense camera with a 1280 by 1024 pixel array was used in conjunction with a NewWave Solo Nd:YAG

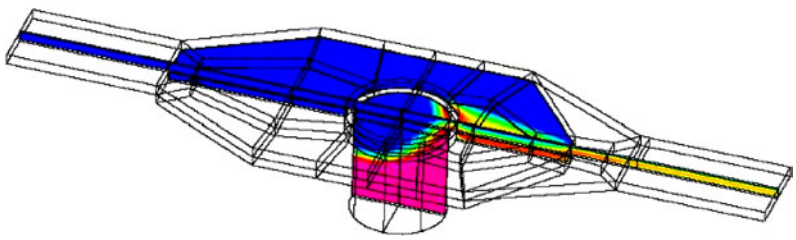

Figure 2. Outline of the chimney structure as modelled with the buffer fluid coming from the left. The shaded contours represent concentration of tracer fluid injected through the chimney illustrating how the buffer fluid laminates the sample fluid in the middle of the exit channel. The buffer to sample volume flow ratio was $R = 25$.

Table 1. Flow setting and key parameters for the cases investigated.

Flow ratio	Inlet flow (ml min^{-1})	Flow in chimney (ml min^{-1})	Flow in exit (total flow) (ml min^{-1})	Maximum velocity in exit (mm s^{-1})	Time between light pulses (μs)
$R = 0.5$	0.01	0.02	0.03	≈24	250
$R = 5$	0.1	0.02	0.12	≈90	60
$R = 25$	0.5	0.02	0.52	≈400	12

laser emitting at $\lambda = 532$ nm. The maximum energy used was 10 mJ. The light from the laser was delivered into the microscope illumination path with an optical fibre fitted to the microscope. The seeding was sufficiently efficient to apply an adaptive (multi-pass) PIV algorithm with 32 by 32 pixel interrogation areas. Only average velocities are presented in the paper. Ensemble correlation, as presented by Meinhart *et al* (1999), was also tested. Although the ensemble correlation is known to provide better results in a sparsely seeded flow, this technique did not provide additional information in our case, apparently because the flow was efficiently seeded.

The imaging was done using an epi-fluorescent microscope (DMLB, Leica) with a 20× /0.40 planachromatic objective and a 0.5× relay lens, resulting in a tenfold magnification and a field of view of 857 by 686 μm. Complementary measurements were also made with a 63 × /0.7 semi-apochromat objective. Both objectives were designed to have a relatively long working distance of up to 3.2 mm and 2.6 mm, respectively, which allowed practical room for the clamping of the holder of the chimney structure. The comparatively thick cover glass of 0.75 mm could be compensated for with adjustable optics integrated in both objectives.

Although oil-immersion objectives are beneficial to the light budget and to the quality of the imaging, these were not applicable in this case due to the fact that the working distances of the oil-immersion objectives were limited to a maximum of 0.22 mm.

With a magnification of 10, the 32 by 32 pixel interrogation area corresponded to 21 by 21 μm. This was a satisfactory size compared to the width of the channel. The focal depth of the microscope objective defines the thickness of the measurement plane. This was calculated to be 16 μm according to Meinhart (2000), which then gives a measurement volume of $21 \times 21 \times 16$ μm^3. Although the 16 μm present a relatively large fraction of the 60 μm channel depth, this was part of a practical trade-off.

The uncertainty of the measurement is estimated to be 0.45 mm s^{-1} for the flow case $R = 5$. The value is justified by observing the rms velocity of the U-velocity component of 50 vector maps in an area of the flow, which can be expected to be undisturbed by actual flow phenomena, i.e. in the vicinity of the walls in the exit channel, where disturbance from the shedding process is small. The value of 0.45 mm s^{-1} corresponds to an absolute uncertainty of 0.04 pixel displacement based on 50 samples. For one single measurement realization, this corresponds to 0.28 pixel ($0.04 \times \sqrt{50}$). This is slightly higher than ordinary PIV experiments, where a typical absolute uncertainty between 0.1 and 0.2 pixel displacement on a single measurement realization can be found. The uncertainty for the two other flow cases in table 1 is estimated to be 0.11 mm s^{-1} and 2.3 mm s^{-1} for the cases $R = 0.5$ and $R = 25$, respectively. The absolute accuracy of the measurement depends on a number of scaling factors, i.e. the optical magnification. A direct indication of the absolute accuracy is seen in table 2 by the fine agreement between the flow rates shown.

Table 2. Volume flow in the exit channel from PIV data and nominal volume flow of the syringe pumps. The PIV based volume flow was derived by integration of the velocities over the area of the exit channel.

Nominal flow rate (ml min^{-1})	Flow rate from PIV data (ml min^{-1})
0.030	0.028
0.12	0.12
0.52	0.48

The PIV measurements were done in two regions as outlined in figure 1. In the exit channel, the measurements were performed at five planes spaced 10 μm apart with the 857 by 686 μm field of view, as shown in figure 3. The first plane was estimated to be located approximately 10 μm below the glass surface, placing the volume that was mapped in the vertical centre of the channel. The 10 μm spacing provides a vertical overlap of 40%, given the focal depth of the microscope of 16 μm. Hence, the vertical overlap was similar to the overlap used for the in-plane PIV processing. Using the velocities from each measurement plane, velocities were extracted in the x–z-plane, as illustrated in figure 3.

The measurement area outlined in figure 1 in the central region around the chimney and upstream towards the step into the exit channel is composed of images originating from several camera positions. From each camera position, the field of view was 857 by 686 μm, resulting in a combined area of 857 by 1646 μm.

3. Stereoscopic micro-PIV measurements

A translation stage was used to map a larger area of the microstructure outlined in figure 1. The stage could also be used to obtain stereoscopic information from the flow in the same manner as cartographic information is gathered by flying over a terrain. In the shaded area of figure 1, two successive camera positions have significant overlap. The translation between these two positions was 320 μm or approximately half of the field of view. Inside the overlapping area, it was possible to perform stereoscopic recombination of the results, assuming the flow was stationary or more precisely that the average of several realizations was stationary. In this case, the flow measured at each camera position was an average of 50 samples, each sample recorded at statistical unrelated times.

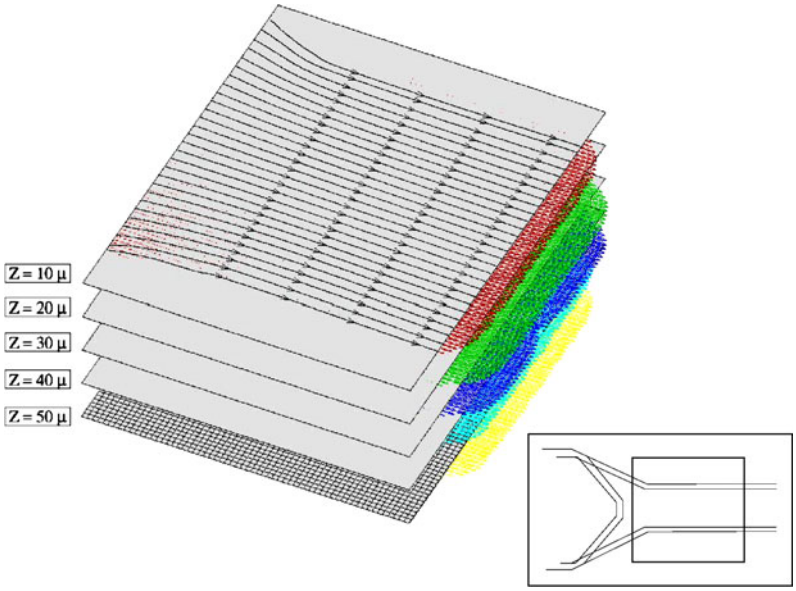

Figure 3. PIV measurements in the exit channel were performed in five x–y-planes spaced 10 μm in depth (z-direction). The measurement area is indicated in the inset. There were 63 by 79 vectors in each plane originating from an interrogation area of 21 by 21 μm. The thickness of the measurement plane was defined by the focal depth of the microscope objective to be 16 μm. Stream traces on the top plane indicate the end of the contraction and the beginning of the exit channel.

The most common technique used to compute stereoscopic PIV results is to pre-calibrate the two camera views with a known calibration target placed at different z-positions. From the calibration a transfer function is generated, which is often a direct linear transform. This approach would also have worked satisfactorily for this application, except for the obvious access problems, making it impossible to position a calibration target *in situ*. Alternatively, an analytical approach could be chosen as described by Prassad and Adrian (1993). The two main parameters are the translation between the camera positions and the optical path from the measurement plane to the principal plane of the optical imaging system. Although the translation was accurately known, the optical path was only known in coarse details.

Mapping the entire parameter set needed for the stereoscopic combination would have been a complicated task. It requires that refraction of light in the air/glass interface of the cover glass on the microstructure be taken into account. In particular, the orientation of the microstructure surface must be well known in order to determine the refraction of light in the cover glass. A scheme to map the various parameters failed in the measurement campaign presented here and therefore a more pragmatic approach was chosen. Ignoring the air/glass interface and pretending the set-up to appear in a medium with a uniform refractive index, the equations for recombination were significantly reduced. Ignoring the interface and cover glass (750 μm thick) seemed reasonable, since it was less than one-third of the optical path from the objective to the measurement plane. Further, the stereo view angle was less than 6° and the imaging was sharp all over the field of view of the camera. Prassad and Adrian (1993) present three equations for fluid displacement in air (equations (11)–(13)). Of these we work with the equation for the z-velocity component:

$$W = \frac{\Delta z}{\Delta t} = \frac{1}{\Delta t}\frac{-d_0(\Delta X_1 - \Delta X_2)}{M_0 S - (\Delta X_1 - \Delta X_2)} \qquad (1)$$

where Δz is the displacement, Δt is the time between the two laser pulses, S is the displacement between the two camera positions, d_0 is the object to lens distance, M_0 is the magnification and ΔX_1 and ΔX_2 are the displacements measured by the camera in the two view positions.

Observing that $M_0 S \gg (\Delta X_1 - \Delta X_2)$, equation (1) may be simplified to

$$W = \frac{d_0}{S}\frac{(\Delta X_2 - \Delta X_1)}{M_0 \Delta t} = \frac{d_0}{S}(U_2 - U_1). \qquad (2)$$

Hence the W-velocity component may be expressed as the difference between the velocities measured from each camera in the translation direction (x-direction) scaled with a factor (d_0/S). This means the W-component may always be visualized qualitatively, and additionally be quantitatively estimated, except for the scaling factor. For this case using a qualified guess, an absolute velocity magnitude was obtained. Compared to the result from computational fluid dynamics shown in figure 7, the factor was underestimated by at least 20%. The correction was included in the PIV plot shown in figure 7.

4. Simulations

Flow in the chimney structure was simulated using the commercial software package CFD-ACE+ 6.4 from CFD Research Corporation, Huntsville, AL, for computational fluid dynamics (CFD). This piece of software is a multi-physics package based on the finite-volume method. The program was run on an 800 MHz Pentium III processor with 512 MB of RAM. Although the experiments were carried out in the laminar flow regime, simulations were done on a fine mesh of about 100 000 cells to account for the complex geometry of the fabricated design. The geometry used in the simulations included some simplifications compared to the actual microstructure used for the experiments. The sidewalls

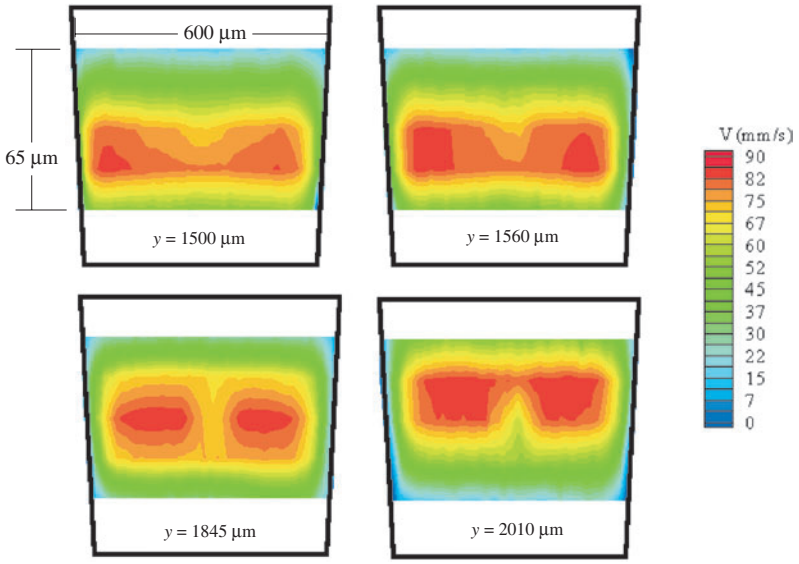

Figure 4. V-velocity component shown in x–z-planes. The data were extracted from the PIV results shown in figure 3 at four y locations. Note that channel height and width are scaled differently. Colour coding of V-component was the same in figures 4 and 6.

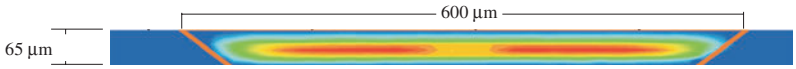

Figure 5. Realistic dimensions of the x–z-planes of figure 4.

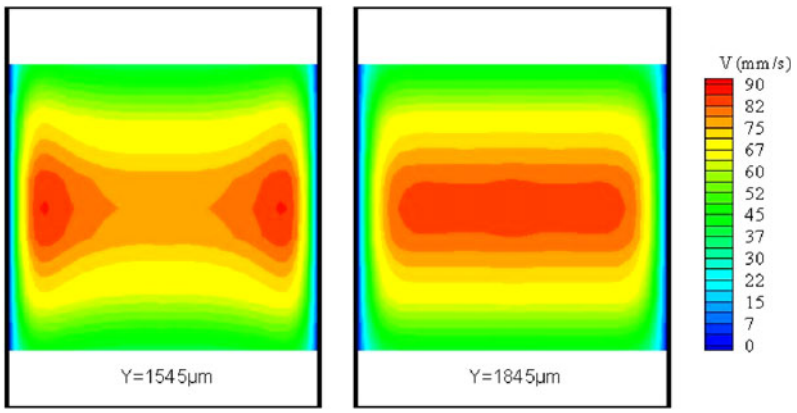

Figure 6. V-velocity component shown in x–z-planes. The data were extracted from the CFD results shown in figure 3 at two y locations. Colour coding of V-component was the same in figures 4 and 6.

of the structure have a slope originating from the underetching during the manufacturing process. This slope was not taken into account in the simulations; i.e. the exit channel was modelled as being rectangular. Furthermore, the width to depth ratio in the exit channel was 7.8, whereas the actual ratio was 9.5. The actual channel dimensions are depicted in figure 5.

The CFD-ACE+ 6.4 software offers several different boundary conditions for the buffer and sample streams to be set, the initial flow rate, the average velocity or the velocity profile. The small dimensions of microsystems usually mean that velocity profiles do not develop fully within the microsystem. Therefore, we chose to run the simulations with both the set flow rates and the average velocities instead of the fully developed profile. Since the results using a set average velocity boundary condition were far more stable, only these are presented in this paper. The known flow rates for buffer and sample stream listed in table 1 were used to derive one set of boundary conditions. The initial velocity of the sheathing stream was set to 44 mm s^{-1} and the velocity of the sample stream was set to 11 mm s^{-1}. Results from the simulations can be seen in figures 6 and 7.

5. Results and discussion

As mentioned above, the measurement volume was about $21 \times 21 \times 16\ \mu m^3$ ($H \times W \times D$). The horizontal dimensions, i.e. the dimensions of the interrogation area, are given by the number of pixels chosen, their size and the magnification of the microscope. The vertical dimension was given by the depth of field of the microscope and depends on the

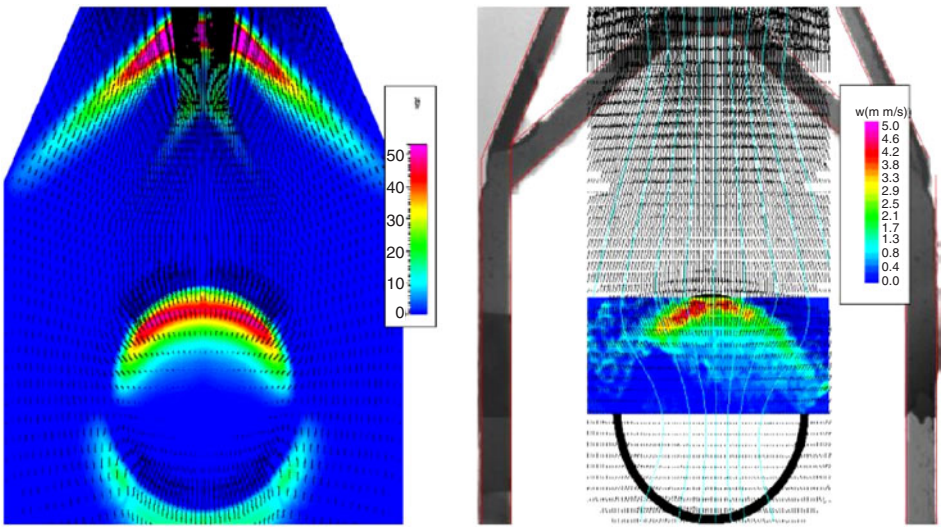

Figure 7. All three velocity components are shown in a plane 30 μm above the chimney. CFD results are shown to the left and PIV to the right. The colour indicates the magnitude of the W-velocity component. In the PIV results, the U, V-velocity vectors were obtained from several camera positions. Stream traces of the U, V-component were shown. The W-component was obtained by combining the results from two overlapping camera positions with a stereoscopic technique.

magnification and the numerical aperture. The higher the magnification of the system the smaller both the interrogation area as well as the depth of field. This means that an increase in magnification produces in principle an overall decreased measurement volume, which would increase the resolution of the PIV measurements.

Nevertheless, opting for an objective with a low magnification has several practical advantages over choosing a high-magnification objective. Low magnification objectives have larger working distances and provide a larger field of view as well as a stronger irradiance onto the light detector. In our set-up it was not easily possible to use a high-magnification objective due to the thick cover glass of the chimney. Apart from this, a second reason for not choosing a high magnification was that the field of view of the system is decreasing with increasing magnification. In our case, the field of view was chosen to cover the entire exit channel width of 600 μm conveniently within one measurement. Therefore, the system magnification for the PIV measurements was set to be tenfold.

This magnification was achieved using a 20 $\times$ /0.40 objective in combination with a 0.5$\times$ relay lens, which is better than using the 10$\times$ /0.25 objective of the microscope, since the higher numerical aperture of the 20$\times$ objective provides a smaller depth of field and an image of higher contrast. The signal strength measured by the detector is given by the irradiance of an imaged particle within the image plane. This irradiance is proportional to the square of the ratio of the numerical aperture to the linear magnification of the chosen objective (Schröder 1998). At a given magnification, a higher numerical aperture value results, therefore, in increased signal strength, which makes the 20$\times$ objective/0.5$\times$ relay lens combination superior to the 10$\times$ objective.

The reliability of the PIV results was examined by comparing the volume flow of the PIV data in the exit channel to the nominal volume flow given by the syringe pumps.

The flow rate was calculated by integration of the velocities over an exit channel cross section, where a standard numerical method (Simpson's rule) was used. A systematical error of about 10% was found, as presented in table 2. The error probably originates from uncertainty in the magnification of the system, since it was not calibrated, and the limited number of planes used for the integration. During all PIV measurements, the flow in the chimney structure was observed to be laminar and without separations, i.e. no convection due to flow separation in the microsystem could be found.

Figures 4 and 6 show the axial velocity in the exit channel at different y locations for $R = 5$. Note that the z-axis in the images is stretched in comparison to the x-axis. A more realistic view of the dimensions is depicted in figure 5.

The PIV data presented in figure 4 show a pair of higher axial velocity streams at all four y locations. The stream pair moves from the bottom of the channel upward passing through the channel. At the same time the two streams were approaching each other slowly up to the point where they begin to join in the last x–z-slice.

The high-velocity stream pair was a result of the five times higher volume flow rate of the sheathing stream interrupted by the sample stream. The highest measured speed of the pair is about 84 mm s^{-1} as indicated by the colour code in figure 4. At first the stream pair flows low in the exit channel, since the sheathing stream acceleration was a result of the reduced cross section at the end of the chimney basin. Within the basin the maximal V-component of the stream velocity was measured to be 78 mm s^{-1}, which is 8% less than the highest speed in the exit channel. Further along the channel, the sheathing stream pair accelerated the sample stream until an equilibrium velocity distribution was reached. This equilibrium profile was not yet fully developed within the measurement range.

The simulated data show similar axial velocity profiles. The cross section at $y = 1545$ μm, in figure 6, contains the high-velocity stream pair, while the downstream cross section

shows the already merged pair. The colour codes that were used in figures 4 and 6 are equal and it can be seen that in both cases the maximum V-component of the stream velocity is the same, about 84 mm s^{-1}. In contrast to the measured cross sections, the high-velocity areas in the simulated cross sections are closer to the sidewalls. Measuring between the highest speed and a speed of about 20 mm s^{-1}, the distance to the sidewall is 40 and 70 μm in the simulations and about 90 μm in the measurements.

There are two main differences between the PIV and simulation results, the facts that the PIV data show a certain asymmetry and that the stream pair merges earlier in the simulations than in the PIV results. The simulated data are necessarily symmetric, since they have been computed in a symmetrical way to save computing power. The measured data on the other hand reflect the fact that the sheathing buffer stream is pushed up at the end of the basin.

The second main difference between the PIV and simulation results was that the stream pair merged about 300 μm earlier in the simulations. While the simulated cross section at $y = 1545$ μm can best be compared to the measured cross section at $y = 1560$ μm, the simulation results show an equilibrium already at $y = 1845$ μm, where the measurements still show two distinct high-speed streams. The reason for the early stream merger in the simulations was due to numerical diffusion.

The speeds of the two sheathing streams and the sample stream differ where the two streams meet. The slower sample stream exerts a viscous drag on the sheathing streams, which flow next to it on both sides. The resulting acceleration of the sample stream can be described as a diffusion of momentum from the high-speed sheathing streams to the slow sample stream. The numerical computing method used in the presented simulations adds an additional equalizing term, which can also be described as a diffusion. This numerical diffusion is an intrinsic part of all numerical calculations. It can only be alleviated by defining a finer mesh or by choosing a different, more complex, method. In both cases a smaller numerical diffusion is bought at the cost of either longer computing time or increased instability. We therefore decided to accept a certain numerical diffusion, which can be found in our results.

The velocity cross sections shown in figure 4 provide information that would otherwise not be easily obtainable without PIV. Although the distribution of the sample flow concentration can be visualized by injecting a dye (Perch-Nielsen *et al* 2001), it is not straightforward to measure the concentration quantitatively. It is even more difficult to make a statement about the flow velocities in the microstructure. PIV on the other hand is designed to measure the flow velocities and with a slight modification of the experiment, the concentration information can be extracted. To achieve this, only the sample flow is seeded with tracer particles, after which it is possible to observe the sample stream qualitatively and quantitatively using the PIV system components.

Observing the chimney structure at different locations with overlapping field of view allowed the construction of a three-dimensional vector field in the area of the actual chimney as shown in figure 7. Both CFD simulation results and PIV measurement results are shown in the figure, where the U- and V-velocity components are rendered as streamlines while the W-velocity components, normal to the plane shown, are encoded in colour. The in-plane velocities were almost zero inside the area of the chimney. In the vicinity of the chimney, the in-plane velocities were in the range of 10 – 20 mm s^{-1} and the flow through the plane (W-component) had a maximum of about 5 mm s^{-1}. The forward flow sped up towards the exit of the basin and reached about 70 mm s^{-1} within the area shown in figure 7.

Since the absolute value of the W-velocity components was adjusted following the CFD results, only the relative PIV measurement results for the W-velocity components can be compared. These results compare reasonably, with the medium W-velocity components between approximately 13 and 30 mm s^{-1} coming up from the chimney in a roughly 530 μm broad and 190 μm long area in the simulation image, while being 480 μm broad and 120 μm long in the measurement image.

Outside the stereoscopic area, the two-dimensional data were also in agreement. From the chimney structure one would expect the average flow velocity to rise somewhere above the actual chimney due to the increase in volume flow and also at the end of the chimney basin, where the cross sectional area decreases. Both speed increases are observed in both the simulation and PIV results. An interesting result of both simulation and PIV measurement was that the highest sample flow velocity was concentrated at the exit-facing rim of the chimney.

In section 3, stereoscopic recombination was discussed and a method was presented to find the scaling factor between the difference in U-component velocities and the W-component velocity. Another approach to find the scaling factor would be to integrate the volume flow over the entire chimney, since the volume flow is known from the pump settings given in table 1. Within the area presented in figure 7, the volume flow is computed to be 0.011 ml min^{-1}. However, the field of view does not cover the entire exit. Using the CFD result, it is seen that the majority (about 80%) of the volume flow exits the chimney within the field of view from the measurement area. Using this fact confirms that the assumed scaling factor was underestimated by more than 20%.

Observing figure 7, it is fairly obvious that the accuracy of the W-velocity component was only limited, given that it was based on the average of 50 samples. The main sources for this large uncertainty are the very small stereoscopic view angles used. The translation of 320 μm corresponds to a stereoscopic view angle of approximately 2×6 degrees, which challenges the accuracy of the measurement. The measurement could be significantly improved by using a higher magnification with shorter working distance, including larger stereo view angles into the measurement. Additionally, a large-format CCD camera could be used to increase the stereoscopic viewing angle, since it allows exploitation of the full viewing capability of the objectives. Finally, more advanced recombination schemes, which take into account the image distortion introduced by the thick cover glass, could be included in the computation of the W-velocity components.

The most desirable measure for improvement of the experimental results would be to equip the examined

microfluidic structure with a thinner cover glass. This would decrease the distortions and make it possible to use objectives with higher numerical aperture. A cover glass thickness of 170 μm would be desirable, since most objectives are designed to be used with such cover glasses.

6. Conclusion

The flow velocities of a microstructure used in cell sorting were mapped in several planes using PIV. The PIV measurements had an adequate resolution and a good field of view. The quantitative results from measurements and simulations were in reasonable agreement, considering the difference in geometry. Furthermore, it was possible to expand the micro-PIV technique to stereoscopic viewing. Combining the stereoscopic technique with mapping of several planes, the possibility of full volume mapping (x, y, z, U, V, W) micro-PIV was demonstrated.

Micro-PIV results can be used to evaluate and validate the simulation results of micro-fluidic flows. In case of the chimney basin, the PIV results support the simulation results. While comparing simulation and PIV data of the exit channel, a certain difference was found, which was helpful as it points out the care that has to be exercised when simulating flow. To improve the agreement between simulation and measurement, the simulation can in principle be improved by using more complex algorithms or by defining a denser mesh at the cost of increased instability or computation time. The measurement can be improved by employing a higher aperture objective, which would increase the viewing angle as well as collect more light. One crucial step towards this end would be the use of a thinner cover glass.

In general, the good agreement between simulation and PIV will allow the simulation software to be used as an efficient tool to speed up the microstructure design cycle.

Acknowledgment

We acknowledge Ulrik Darling Larsen, whose chimney structure we used in our PIV measurements.

References

Goranović G, Perch-Nielsen I P, Larsen U D, Wolff A, Kutter J P and Telleman P 2001 *Proc. 4th Int. Conf. on Modeling and Simulation of Microsystems (March, Hilton Head Island, USA)* pp 242–5

Larsen U D 2000 Micro liquid handling—passive microfluidics *PhD Thesis* Technical University of Denmark, Lyngby, Denmark pp 93–104

Meinhart C D, Wereley S T and Gray M H B 2000 *J. Fluids Eng.* **122** 285–9

Meinhart C D, Wereley S T and Santiago J G 1999 *Exp. Fluids* **27** 414–9

Perch-Nielsen I P, Goranović G, Klank H, Larsen U D, Wolff A, Kutter J P and Telleman P 2001 *Proc. 5th Int. Conf. on Miniaturized Chemical and Biochemical Analysis Systems (October, Monterey, USA)* pp 629–30

Prassad A K and Adrian R J 1993 *Exp. Fluids* **15** 49–60

Schröder G 1998 *Technische Optik* 8th ed (Würzburg: Vogel) p 77

Tashiro K, Sekiguchi T, Shoji S, Funatsu T, Masumoto W and Sato H 2000 *Proc. 4th Int. Symp. on Micro Total Analysis Systems (May, Enschede, The Netherlands)* (The Hague: Kluwer) pp 209–12

Wolff A, Larsen U D, Friis P and Telleman P 2000 *Proc. 14th European Conf. on Solid-State Transducers (August, Copenhagen, Denmark)* pp 235–8